

JGR Solid Earth

-

RESEARCH ARTICLE

10.1029/2022JB025035

Key Points:

- Stochastic tomography can capture higher order phase and chemical changes undetectable from reflection imaging
- The heterogeneity spectrum of the upper mantle is marked by peaks associated with depth regions undergoing phase or compositional change
- The upper mantle beneath the western US is consistent with a history of subduction and slab stagnation in the transition zone

Correspondence to:

V. F. Cormier, vernon.cormier@uconn.edu

Citation:

Cormier, V. F., Lithgow-Bertelloni, C., Stixrude, L., & Zheng, Y. (2023). Mantle phase changes detected from stochastic tomography. *Journal of Geophysical Research: Solid Earth*, 128, e2022JB025035. https://doi. org/10.1029/2022JB025035

Received 22 JUN 2022 Accepted 24 JAN 2023

Author Contributions:

Conceptualization: Vernon F. Cormier Data curation: Vernon F. Cormier, Carolina Lithgow-Bertelloni, Lars Stixrude

Formal analysis: Vernon F. Cormier Funding acquisition: Vernon F. Cormier Investigation: Vernon F. Cormier Methodology: Vernon F. Cormier, Carolina Lithgow-Bertelloni, Lars Stixrude, Yingcai Zheng Project Administration: Vernon F.

Cormier
Resources: Vernon F. Cormier
Software: Vernon F. Cormier, Carolina
Lithgow-Bertelloni, Lars Stixrude,
Yingcai Zheng

Supervision: Vernon F. Cormier

© 2023. The Authors.

This is an open access article under the terms of the Creative Commons Attribution License, which permits use, distribution and reproduction in any medium, provided the original work is properly cited.

Mantle Phase Changes Detected From Stochastic Tomography

Vernon F. Cormier¹, Carolina Lithgow-Bertelloni², Lars Stixrude², and Yingcai Zheng³

¹Department of Physics, University of Connecticut, Storrs, CT, USA, ²Department of Earth and Planetary Sciences, University of California, Los Angeles, CA, USA, ³Department of Earth and Atmospheric Sciences, University of Houston, Houston, TX, USA

Abstract Stochastic tomography, made possible by dense deployments of seismic sensors, is used to identify phase changes in Earth's mantle that occur over depth intervals. This technique inverts spatial coherences of amplitudes and travel times of body waves to determine the depth and dependence of the spatial spectrum of seismic velocity. This spectrum is interpreted using the predicted thermodynamic stability of mineral composition and phase as a function of temperature and pressure, in which the metamorphic temperature derivative of seismic velocities is used as a proxy for the effects of heterogeneity induced in a region undergoing a phase change. Peaks in the temperature derivative of seismic velocity closely match those found from applying stochastic tomography to elements of Earthscope and Flex arrays. Within ±12 km, peaks in the fluctuation of P velocity at 425, 500, and 600 km depth beneath the western US agree with those predicted by a mechanical mixture of harzburgite and basalt, 180 K cooler than a 1600 K adiabat in the mantle transition zone. A broad peak at 250 km depth may be associated with chemical heterogeneity induced by dehydration of subducted oceanic sediments, and a peak at 775 km depth with a phase change in subducted basalt. Non-detection of predicted phase changes less than 10 km in width is consistent with the resolution possible with the seismic arrays used in the inversion, including the sharp endothermic phase change near 660 km. These interpretations are consistent with the known history of plate subduction beneath North America.

Plain Language Summary The speed of seismic waves in a rock depends on the chemistry and arrangement of the atoms making up the minerals in the rock. These atoms are arranged in different ways, depending on temperature and pressure. Increasing pressure with depth in Earth squeezes the atoms of minerals into denser arrangements. An abrupt change with depth in the arrangement of mineral atoms, termed a phase change, can speed up, slow down, and scatter earthquake waves in different directions, changing their arrival times and amplitudes. This study describes a way in which the fluctuations in the arrival times and amplitudes of seismic waves, recorded by dense collections of seismometers, can be used to locate, detect, and image the depth and thickness of mineral phase changes in Earth's mantle. These phase changes are found to control much of the observed scattering of seismic waves in Earth's mantle from distant earthquakes and agree with the history of plate tectonics of western North America.

1. Introduction

1.1. Observed and Predicted Phase Changes

The best-known solid phase changes in Earth's silicate mantle are commonly detected from the reflection and conversion of body waves interacting with sharp, near discontinuous, changes in velocity and density occurring at or near 410 and 660 km depth (e.g., Niu et al., 2005; Shearer, 1991). These phase changes also produce multi-pathed body waveforms between 15° and 35° great circle range (e.g., Burdick & Helmberger, 1978; Chu et al., 2012). The steepness of the inferred P and S velocity gradients between 410 and 660 km in reference Earth models, however, cannot be explained by plausible silicate mantle chemistry without the existence of at least one more phase change between 410 and 660 km (Anderson, 1989). When the tools of mineral physics are applied to a constrained composition of the Earth's mantle, up to two additional phase changes are predicted to occur between the 410 and 660 km. Several other phase changes are also predicted above and below this zone, each having a unique behavior in their Clapeyron slope and the widths in depth over which each occurs (Figure 1). The widths of more than half of these are on the order of 15–60 km (e.g., Stixrude & Lithgow-Bertelloni, 2007, 2011, 2012), some expressed primarily by changes in velocity gradient, making them difficult to detect from reflected and converted body waves having similar or shorter wavelengths. As demonstrated in Figure 1, the parameterization

CORMIER ET AL. 1 of 15

Validation: Vernon F. Cormier, Carolina Lithgow-Bertelloni, Lars Stixrude, Yingcai Zheng

Visualization: Vernon F. Cormier Writing – original draft: Vernon F.

Cormier

Writing – review & editing: Vernon F. Cormier, Carolina Lithgow-Bertelloni, Lars Stixrude, Yingcai Zheng of reference Earth models by first order discontinuities separating regions of near constant gradient is inadequate in fully characterizing the predicted effects of phase changes.

1.2. Methods for Detection and Analysis

Thermodynamic modeling and mineral physics experiments have largely concentrated on matching average seismic velocities within or near the boundaries of the mantle transition zone between 400 and 660 km phase changes. Research has been motivated by the need to understand spatial scales of chemical heterogeneity observed in magmas, the origin and rheology of the low velocity zone that enables plate decoupling, buoyancy differences between compositions, and mass exchanges between upper and lower mantle (e.g., review by Frost (2008)). Success has been achieved in constraining chemistries that match observed seismic velocities over a broad region of depth. With increasing degrees of sophistication, thermodynamic models examining effects of compositions in the form of either mechanical mixtures or solid solutions have succeeded in matching average elastic velocities, their gradients with depth, and mineral phase changes in the transition zone (e.g., Buchen, 2021; Cammarano et al., 2005; Chust et al., 2017; Stixrude & Lithgow-Bertelloni, 2011; Wang et al., 2018; Xu et al., 2008).

In contrast to constraining chemistry or temperature over a broad region of depth, our objective in this paper is to illustrate a new technique to determine the rate of mineral phase changes over very narrow intervals of depth. This objective has been difficult in studies of receiver functions (Vinnik, 2019) and precursor underside reflections (e.g., Koroni & Trampert, 2015; Xu & Vidale, 2003) because it requires measuring the frequency dependence of body wave reflections and conversions from band-limited data from stacked body waves having variable frequency content. In both receiver function and precursor studies the effect of travel time fluctuations due to unresolvable, small-scale, 3-D structure, which we exploit in the methods of this paper, can diminish the amplitude of reflections and P to S conversions in stacked seismic traces (e.g., van Stiphout et al., 2019).

1.3. A New Opportunity

A serendipitous discovery from the inversion of P wave coherences across the USArray (Cormier et al., 2020) reveals that many of these phase changes are marked by peaks in the depth-dependency of the spectrum of mantle heterogeneity (heterospectrum) that correlate with peaks in the temperature derivatives of seismic velocities predicted by thermodynamic models of mantle composition and phase. A heterospectrum is the spatial Fourier transform of the seismic velocity (or density) perturbation field at a depth relative to a reference model. It measures the squared Fourier amplitude as a function of the 'spatial frequency' (commonly known as the spatial wavenumber, $k = 2\pi/a$, where a is the heterogeneity spatial period/scale/size).

Stixrude and Ligthgow-Bertelloni (2005, 2007) have demonstrated that small lateral variations in temperature (<150 K) allow the peaks in the predicted temperature derivatives to capture the depth zone in which two competing mineral phases may coexist in a heterogeneous mixture that is capable of scattering seismic body waves (Figure 2). These peaks in the metamorphic component of the temperature derivatives can be used to identify and interpret peaks in narrow depth ranges of the mantle heterospectrum. This heterospectrum can be inverted from fluctuations in travel time and amplitudes of transmitted seismic waves observed across dense networks of seismic stations by a process known as stochastic tomography.

1.4. Organization

In Section 2 we begin by reviewing the depth-dependent heterospectrum of *P* wave velocity beneath the western US determined by the stochastic tomographic inversion of Cormier et al. (2020). In that study we inverted observed fluctuations in P wave amplitudes and travel times for a P velocity heterospectrum and qualitatively compared it with a heterospectrum predicted from the thermodynamic code HeFESTo Stixrude & Ligthgow-Bertelloni, 2005, 2007). We did not attempt, however, to quantitatively fit a thermodynamically predicted P heterospectrum to a seismologically inverted P heterospectrum, nor did we correct for effects of differences in the sensitivities to heterogeneity scale length between the stochastic tomographic inversion and HeFESTo modeling. This is now done in Section 3, which describes how to process the predictions of a thermodynamic code so that they have same sensitivity to heterogeneity scale length as a stochastic tomographic inversion.

In Sections 4 and 5, we interpret the inverted *P* spectrum with estimates of uncertainties of phase change depths and their widths obtained for the mantle beneath the western US sampled by our data. Signified by an observed

CORMIER ET AL. 2 of 15

21699356, 2023, 2, Downloa

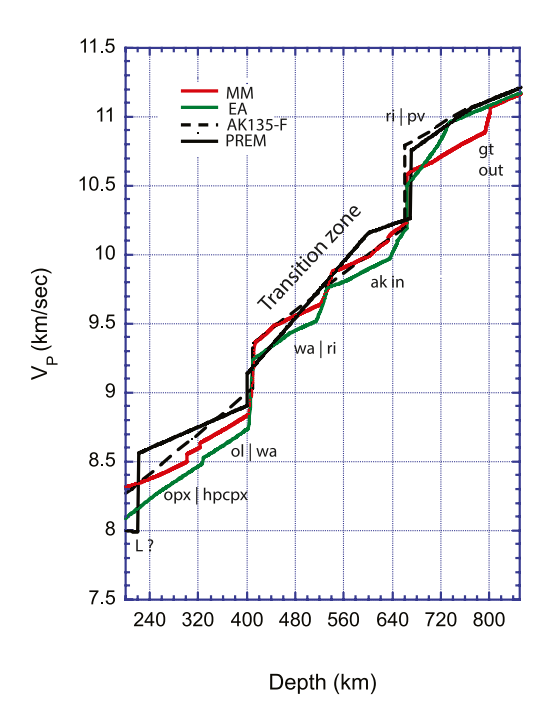


Figure 1. *P* velocities of reference Earth models and predictions from the thermodynamic modeling code HeFESTo for varying compositions and geotherms. Reference Earth models plotted in black are PREM (Dziewonski & Anderson, 1981) and AK135-F (Montagner & Kennett, 1995). Colored lines are HeFESTo's prediction for an equilibrium pyrolite composition (EA) for a 1600 K isentrope of Stixrude and Lithgow-Bertelloni (2011), and for a mechanical mixture of 80% harzburgite and 20% basalt composition (MM) for the isentropes of Katsura (2022). Sharp change in velocity or its slope with depth are labeled for HeFESTo's predicted phase changes in silicate minerals. These are orthopyroxene to high pressure clinopyroxene (opx | hpcpx), olivine to wadsleyite (ol | wa), wadsleyite to ringwoodite (wa | ri), the appearance of akimotoite (ak in), ringwoodite to perovskite (ri | pv), and the disappearance of garnet (gt out). A sharp change in *P* velocity at 220 km in the reference model PREM (L?) is not associated with a HeFESTo predicted or known change in phase.

shift in depth of the wadsleyite to ringwoodite phase transition from that predicted by a mantle adiabat, we propose a possible perturbation of the upper mantle geotherm due to stagnation of the Farallon slab in the transition zone.

2. Stochastic Tomography

2.1. Method and Data

Small-scale heterogeneities, unresolvable by conventional tomography, have detectible signatures in the fluctuation of amplitudes and travel times observed across seismic arrays (Wu & Flatté, 1990). Numerical simulations have shown that small-scale heterogeneity in the upper mantle can affect the wavefront of an incident teleseismic wave beneath an array (Zheng & Wu, 2008). Small differences in the angle of approach of wavefronts, on the order of a several degrees or less, can produce unique signatures in amplitude and phase fluctuations due to differences in the sensitivity of the wavefronts to small-scale structure (e.g., Tkalčić et al., 2010). Measurement of these fluctuations from the coherence between array elements can be exploited to invert for the spectrum of heterogeneity beneath the array with techniques that have been named stochastic tomography (Wu & Xie, 1991; Zheng & Wu, 2008).

Coherence measures the similarity of amplitude and travel time between body waves received by two adjacent receivers separated by a specific distance, commonly termed a lag. In the frequency domain, travel time differences are included by measuring the phase ϕ given by the product ωt of radian frequency and travel time. Stochastic tomography, which approximates the interference effects of single scattering in the forward direction, constructs coherences to measure the similarity of the natural log of the ratio of the observed to predicted amplitude and observed to predicted phase in a reference Earth model (Appendix A). As the lag distance between two stations approaches zero, amplitude coherence approaches 1 and phase coherence approaches 2π or 0. As the lag distance between pairs of receivers increases amplitude and phase coherence decrease due to the constructive and destructive interference of single scattered waves, for example, Figure 3.

2.2. Resolution of Scale and Depth Dependence

The 10–20 km spacing of the denser permanent US networks and Flex arrays shown in Appendix B, suggest the possibility of achieving a similar sized resolvable scale length of heterogeneity from the inversion of synthetic data. In such a study, Wu and Xie (1991) applied a stochastic tomographic inversion to numerically synthesized seismograms in media having known depth-dependent heterogeneity spectra in the presence of noise. For coherence inversions that combined wavefronts arriving from different angles (e.g., Figure 4) they found it possible to achieve a depth resolution equal to the spacing of sensor elements. Together with damping near site effects by averaging many paired coherences for each lag interval plotted in Figure 3, this enhancement of depth resolution motivated our choice for jointly inverting the coherences for the three epicentral groups of deep focus earthquakes described in Appendix B, whose ray paths arrive at different azimuthal and vertical angles.

2.3. Single Layer Inversion

As a first step it is useful to factor out the wavenumber dependence from a depth dependent spectrum and compare its spectrum against published, non-depth dependent, stochastic models of upper mantle heterogeneity. We thus first inverted for a uniform heterogeneity spectrum with depth in which the shape of the power spectrum in wavenumber was defined by 4 parameters, consisting of a fractional velocity fluctuation, an upper

CORMIER ET AL. 3 of 15

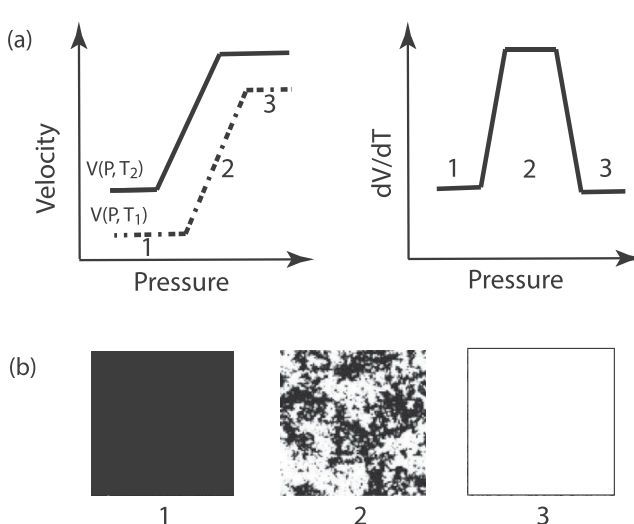


Figure 2. (a) Illustration of how a change in seismic wave velocity (P or S) over a zone of exothermic phase change affects its temperature derivative assuming a positive Clapeyron slope. Top left: the solid line is velocity as a function of pressure at a temperature T_2 and the dotted line is the velocity as a function of pressure for a higher temperature T_1 . Top right: difference derivative of velocity as a function of pressure with respect to temperature, $|V(P, T_2) - V(P, T_1)|/[T_2 - T_1]$ (b) Possible textures of a mineral changing from the white phase to the black phase in the pressure (depth) regions labeled 1, 2, and 3 in (a).

and lower correlation length scale, and a Hurst number (e.g.,Klimes, 2002; Sato et al., 2012). Figure 5a compares our inverted spectrum for the upper 1,000 km of the mantle to an overlapping band of wavenumbers estimated by Mancinelli et al. (2016) from the low-frequency (<0.2 Hz) scattered coda of teleseismic body waves. The two spectra nearly coincide in a narrow wavenumber band centered near 0.065 km⁻¹. The dominant frequency (0.7 Hz) of our *P* wave data in this wavenumber corresponds to a 100 km wavelength in the upper mantle. At this center frequency, scattering will primarily be the Mie type in the forward direction, with sensitivity strongest to velocity rather than impedance heterogeneities having a scale between 10 and 100 km. A minimum detection threshold of 10 km scale agrees with the highest resolution achievable by stochastic tomography with our smallest sensor spacings. It also agrees with our detections and non-detections of phase changes predicted from thermodynamic modeling (Section 3).

2.4. Depth Dependent Inversion

We next assumed that the shape of the heterogeneity power determined from the single layer inversion (Figure 5a) was constant in depth but allowed its spectral amplitude to vary with depth in a stack of uniformly thick layers. The thickness of each layer was decreased as long as a reduced χ^2 a measure of the misfit between and predicted coherences remained greater than 1. The smallest reduced χ^2 greater than 1 occurred for the case of 40, 25 km thick, layers. Figure 5b plots the inverted depth dependence of P velocity fluctuation. Compared to the uniform model, the squared coefficient of determination of coherences for the depth dependent model increased from 0.74 to 0.80. The reduced χ^2 computed from observed and predicted coherences

decreased from 1.65 to 1.05. The significantly smaller, but not less than 1, χ^2 for the depth dependent spectrum is consistent with an improved fit, but not an over-fit due to the assumption of a larger number of unknown parameters.

3. HeFESTo: A Thermodynamic Model of Mantle Composition and Phase

3.1. Temperature Derivatives of Seismic Velocity

HeFESTo is a Fortran code for computing seismic velocities, densities, and other physical properties for silicate minerals that minimize the Gibbs free energy at specific temperatures and pressures (Stixrude & Ligthgow-Bertelloni, 2005, 2007, 2022). Its input consists of pressure, temperature, and a bulk composition in the SiO₂-MgO-FeO-Al₂O₃-CaO-Na₂O system, and models of the properties of 51 end-members of 22 phases and their interactions. Among its output options are elastic velocities and density, as a function of depth. Isomorphic (constant phase) temperature derivatives of elastic velocity are calculated analytically. The additional contribution of a metamorphic component in the midst of a solid phase change can be calculated from difference derivatives determined by running the code at two closely spaced temperatures (e.g., Figure 2a and Stixrude & Lithgow-Bertelloni, 2007). In the results shown in this paper, we calculated difference derivatives of dlnVp/dT to double precision on a 64-bit processor, assuming either adiabatic or isothermal conditions and two temperatures separated by 10 K.

3.2. The Metamorphic Temperature Derivative as a Proxy for Heterogeneity

Because the slope of the boundary between two stable silicate phases in P-T space is neither zero nor infinite, any lateral change in temperature will also be associated with a change in the pressure (depth) of the phase boundary. This makes it possible for the temperature derivative of to be used as a proxy for locating and measuring the width of a zone in which the two phases are competing for equilibrium (e.g., Figure 2a). Stixrude and Lithgow-Bertelloni (2007) have termed the temperature derivative of velocity in this situation the metamorphic derivative in recognition that its shape is affected by more than one form or phase of a mineral. The existence

CORMIER ET AL. 4 of 15

21699356, 2023, 2, Downloaded from https://agupubs.onlinelibrary.wiley.com/doi/10.1029/202218025035 by University of California - Los Ange, Wiley Online Library on [26/06/2023]. See the Terms and Conditions

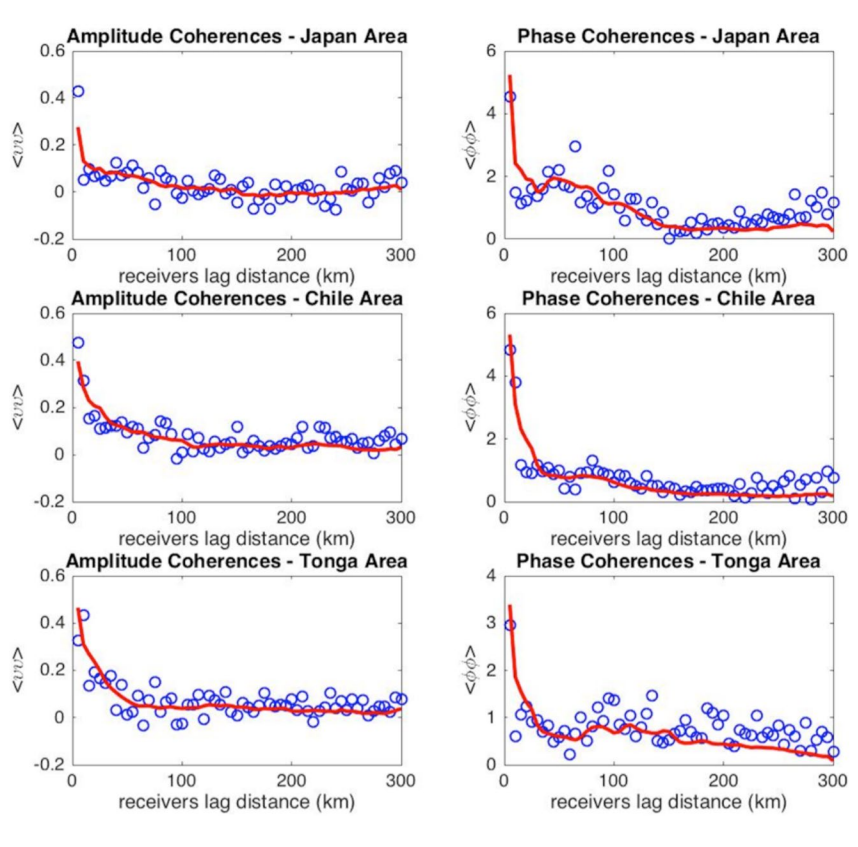


Figure 3. P wave log-amplitude and phase coherences are plotted for seismic stations in western North America between 30°N and 50°N latitude and 100°W to 125°W longitude, summed over all possible pairs of stations at specific lag distances (open circles); predicted P wave coherence (solid lines) for a depth dependent model of mantle heterogeneity power spectra (Cormier et al., 2020).

of two phases in the zone of the phase transition, with differing seismic velocities and density can scatter body waves. Hence, peaks in the predicted metamorphic component of the temperature derivative of a seismic velocity will be associated with peaks in the heterogeneity spectrum as a function of depth.

Implemented as a proxy for seismic velocity fluctuations, the values of $d\ln Vp/dT$ require a multiplication by a factor related to the mean lateral temperature variation to convert them to estimates of the mean fluctua-

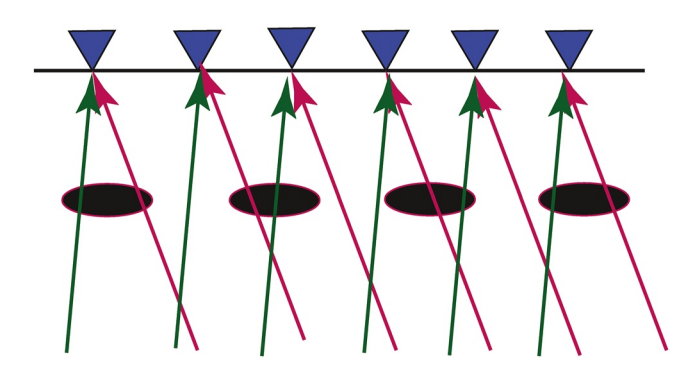


Figure 4. Illustration of how incorporation of wavefronts arriving from different directions (red and green arrows) can enhance the resolution of small-scale heterogeneities (black ellipses). Blue triangles are seismic stations on the Earth's surface. Depth resolution is possible because heterogeneities at different depths cast different "shadows" (fluctuations of wavefront) observed on the Earth's surface.

tions of P velocity, $\Delta Vp/Vp$. Stixrude and Lithgow-Bertelloni (2012) find that an upper bound of 150 K for lateral temperature variations agrees with the magnitudes of velocity variations observed from seismic tomography in the upper mantle. A temperature difference as high as 500 K has been estimated between a slab and plume in the Tonga-Samoa region (Li et al., 2019), representative of the difference between two extreme domains rather than the mean of lateral variations in temperature under the US continent. Although velocity variations inferred from tomography are likely underestimates, Solomon (1976) separately argues for 150 K lateral temperature variations from geodynamic considerations. An alternative estimate of this conversion factor, not related to any assumption of lateral temperature differences, is to estimate the maximum velocity fluctuation across the phase transition zone between two competing phases. This is simply the difference in velocities between two depth sides of a phase change divided by the average of the two velocities. For the 410 km phase change, this value is 3% from the HeFESTo estimated velocity changes for both pyrolite and harzburgite/basalt mixtures. This leads to the identical conversion factor of 150 K at 410 km. We apply a slightly more conservative estimate of 100 K from comparing the scale of

CORMIER ET AL. 5 of 15

.com/doi/10.1029/2022JB025035 by University of California

- Los Ange, Wiley Online Library on [26/06/2023]. See the

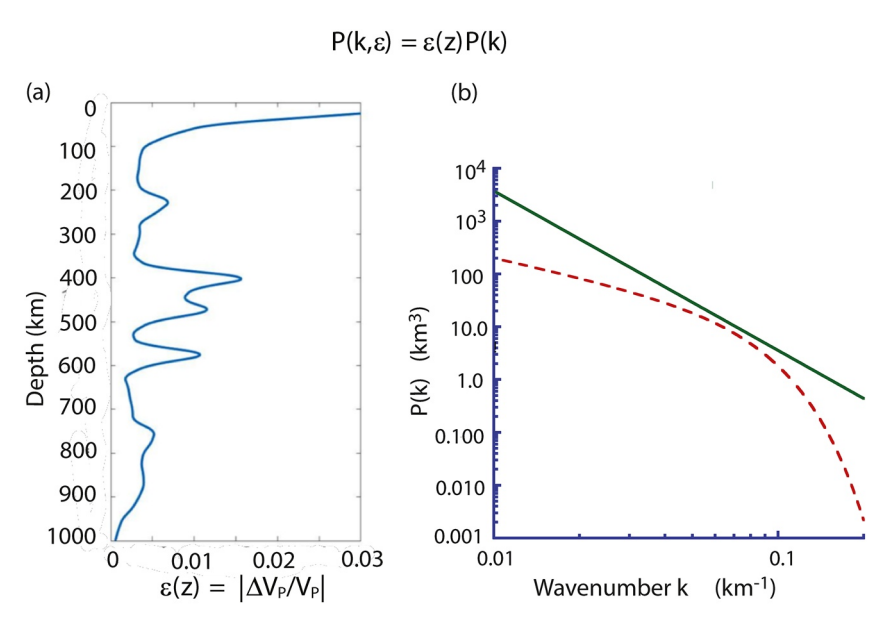


Figure 5. Power spectrum of the root-mean-square (RMS) fluctuation of P wave velocity specified as a product of two functions derived from stochastic tomography (Cormier et al., 2020): (a) a non-dimensional function ε of depth for the fractional RMS fluctuation of P velocity as a function of depth, smoothed over 40 discrete depths spaced 25 km apart; and (b) a power spectrum density P(k) and as a function of wavenumber k for the upper 1,000 km of Earth's mantle determined from stochastic tomography (dashed red line), compared with Mancinelli et al.'s (2016) estimates for this depth range in the frequency band of teleseismic body waves (solid green line).

P velocity variations (order of 1%) inferred from P travel time tomography to thermodynamic estimates of the isomorphic temperature derivative (the temperature derivative not in a region of a phase change). Given the existence of uncertainties in the lateral temperature differences and the precise shape of the heterogeneity spectrum and its variation across the zone of a phase change, we estimate that the true magnitude of P velocity fluctuations within most of the phase changes occurring over zones wider than a wavelength is likely to lie between 1% and 3%.

3.3. Resolution Possible From Stochastic Tomography

A phase change that occurs over a depth range less than 8 km wide is unlikely to be detected as narrow zone of increased heterogeneity for sensor spacings between 10 and 20 km. The 660 km phase change from ringwoodite to bridgmanite and ferropericlase is predicted by HeFESTo to be 1–2 km wide in agreement with both other computational and experimental estimates in mineral physics (e.g., Ishii et al., 2019). Another phase change near 300 km depth from ortho-pyroxine to high pressure clino-pyroxene (opx | hcpx) is also quite narrow. The thermodynamic code HeFESTo predicts it to occur over 8 km. Such phase changes occurring over depth zones less than 10 km width are easily detected from reflected and converted body waves. This is especially the case for 660 km phase change, which has been observed in reflections at 1–2 Hz. The non-detection of the 660 and 300 km phase changes in our stochastic tomography inversions, sensitive to phase changes wider than 6 km, is consistent with their narrowness.

To facilitate comparison with the thermodynamic code we first isolate the HeFESTo predicted phase changes that are wide enough to be detected by stochastic tomography. To achieve this, we first apply a median filter to the HeFESTo predicted phase changes from metamorphic temperature derivatives, and then apply a spatial averaging equal to the observed lag intervals of coherence. The input parameters describing this median filter, often used to remove electronic spikes in seismic recordings (Evans, 1982), were chosen to remove all signals in the metamorphic derivatives that are less than 6 km wide. Figure 6 shows an example in which the two steps of median filtering and spatial averaging have been applied to the HeFESTo predicted temperature derivatives of P velocity. Note that median filtering removes narrow peaks without much distortion in the shape of the signal,

CORMIER ET AL. 6 of 15

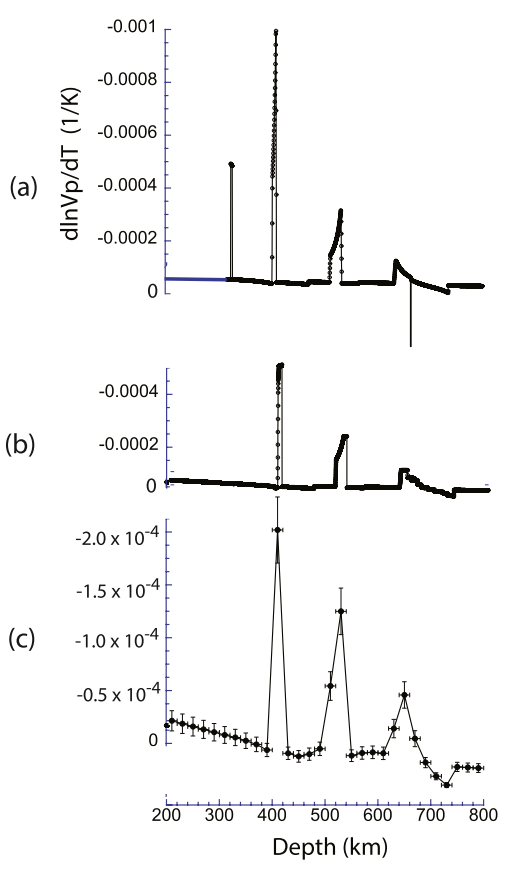


Figure 6. (a) HeFESTo $d\ln Vp/dT$ computed for a pyrolite model of the upper mantle; (b) followed by median filtering applied to (a) to remove signals less than 6 km wide; and (c) followed by 20 km wide depth averaging applied to (b).

while averaging values over a depth interval acts more like a simple lowpass filter in wavenumber, strongly reducing amplitudes and widening peaks.

4. Results

4.1. Interpretation of the Depth Dependent Heterogeneity Spectrum

Results of our inversion for a depth dependent heterogeneity spectrum for the upper 1,000 km of the mantle beneath the western US for the root-mean-square (RMS) P velocity fluctuations are shown in Figure 7. These are compared with the HeFESTo predictions for P velocity fluctuations derived from the temperature derivatives of P velocity. The HeFESTo predictions, for both an equilibrium pyrolite composition (EA) and a mechanical mixture of harzburgite and basalt (MM), are filtered and averaged to agree with the estimated sensitivities of stochastic tomography (Section 3). For the P velocity fluctuation predicted from stochastic tomography, the horizontal uncertainty bars in depth in Figure 7 are fixed at 25 km in length to represent the spacing between averaged coherence lags. For the P velocity fluctuations estimated from HeFESTo, the horizontal uncertainty bars are the width of a 20 km moving depth average of the filtered temperature derivative of velocity. Vertical bounds on peaks were found by varying the starting depth of the moving average. Variations in the peak height were found to be equal to or smaller 10% of the median peak value calculated from the changes in peak height due to assuming different starting depths of the moving average.

The HeFESTo predicted peaks in the temperature derivative of seismic velocities are from metamorphic contributions due to changes in constituent mineral phases required to minimize Gibbs free energy. Computer runs are shown for an equilibrium pyrolite model and a mechanical mixture of harzburgite and basalt to simulate the effects of slab cycling. The expression of phase changes can either be sharp or spread out over a depth range bounded by two changes in the gradient of seismic velocity. If sharp (less than 10 km in width), the phase change can be easily detectable from

reflected, converted, or multi-pathed body waves. In these cases, the effect of lateral temperature variations will be expressed as topography on an apparent seismic reflector rather than a zone of increased heterogeneity. The predicted phase change at 660 km of ringwoodite to Mg-perovskite and magnesiowustite is one such example. Phase changes wider than 10 km in depth may not be detectable in seismic reflections or receiver functions but will be detectable from stochastic tomography as a zone of discrete scatterers in a narrow range of depth close to the width of a peak in the filtered HeFESTo prediction for the temperature derivative of P velocity. For these phase changes, the horizontal length scale of the scatterers will be related to the lateral scale of temperature variations and the vertical scale to the width of the depth (pressure) range over which the phase change occurs.

4.2. Largest Peaks in the Depth Dependent Heterogeneity Spectrum

The depths and relative amplitudes of at least three of the peaks in the heterogeneity spectrum measured by stochastic tomography agree well enough with those predicted by HeFESTo to have confidence in an identification of the detected phase change. These are:

- 1. A peak at 425 ± 12 km depth nearly matches a HeFESTo predicted phase change of olivine to wadsleyite (ol | wa) at 412 km occurring over a 10 km width.
- 2. A peak at 500 ± 12 km depth matches a HeFESTo predicted phase change of wadsleyite to ringwoodite (wa l ri) at 500 km occurring over 20 km width.
- 3. In mechanical mixtures of harzburgite and basalt (MM), a peak at 600 ± 12 km matches the interference of two predicted phase changes, each exothermic with positive temperature derivatives of velocity. Together they occur over a 30 km width. In equilibrium pyrolite, these phase changes are predicted to be deeper at 640 km depth.

CORMIER ET AL. 7 of 15

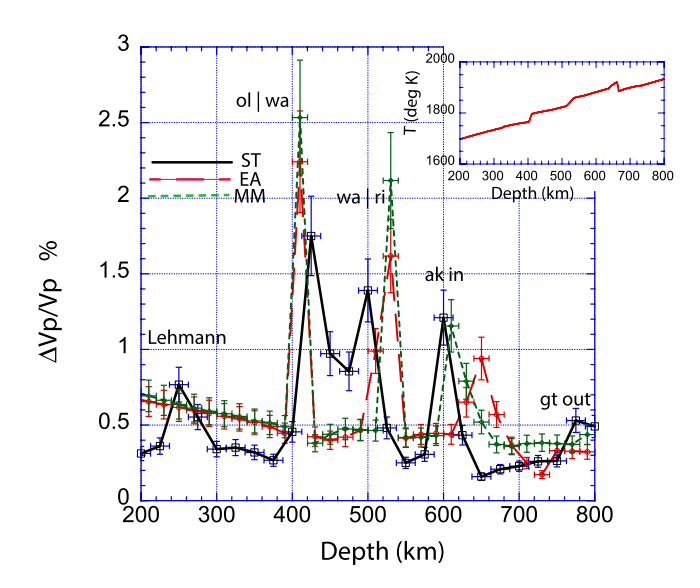


Figure 7. Solid black line (ST): the depth dependent heterogeneity spectrum for the root-mean-square fluctuation of *P* wave velocity in the upper 1,000 km of the mantle estimated from stochastic tomography. Long dashed red line (EA): filtered temperature derivative of *P* velocity predicted for an equilibrium pyrolite model. Short dashed green line (MM): filtered temperature derivative of *P* velocity predicted for a mechanical mixture of 80% harzburgite and 20% basalt. Each thermodynamic prediction assumes an adiabatic temperature profile having a 1600 K potential temperature (inset upper right). Interpreted detections of the Lehmann discontinuity and upper mantle mineral phase changes are labeled above or near peaks.

At 600 km depth the predicted signal in the temperature derivative of velocity consists of a relatively wide peak in which the shallower wadsleyite to ringwoodite phase change interferes with an initiation of a deeper calcium perovskite phase (capv in). The 600 km initiation of akimotoite is not the deeper endothermic phase change associated with the sharp discontinuity commonly detected near 660 km. For some compositions and temperatures, HeFESTo predicts the 660 km phase change to occur over two sharp, and closely spaced depths. These two deeper phase changes are too sharp to be detected by stochastic tomographic with the array and frequency band of this study. Both seismic observations and mineral physics studies (e.g., Ishii et al., 2019), predict a 660 km deep phase change to occur over a zone equal to or less than 2 km. In the median filtered and moving averaged HeFESTo predictions shown in Figure 6c and the dashed lines in Figure 7 the phase changes near 660 km vanish, but appear in the unfiltered HeFESTo prediction shown in Figure 6a.

If our estimated error bars in depth are close to truth, the 600 km phase change detected from stochastic tomography is in better agreement with our tested mechanical mixture of harzburgite and basalt rather than a pyrolite composition in the mantle transition zone. Within error bars, our stochastic tomography detection at 500 km depth for the wadsleyite to ringwoodite phase change is shallower than either the HeFESTo predictions for either pyrolite or a mechanical mixture. The disagreement is similar for both compositional models, suggesting that a better agreement may be achieved either by revising the HeFESTo inputs for the physical properties of individual minerals or by revising the temperature profile. Of these two choices, the depth of phase changes is more sensitive to the temperature profile. In Section 5, we discuss how a negative temperature perturbation in the 410–660 km transition zone,

consistent with a history of subduction, can bring the observed and predicted heterogeneity spectra into closer agreement.

4.3. Smaller Peaks in the Depth Dependent Heterogeneity Spectrum

4.3.1. 775 km

Another peak requiring a small negative perturbation to an assumed adiabatic temperature profile is a peak at 775 ± 12 km. This peak nearly correlates with a HeFESTo predicted phase change at 795 km in mechanical mixtures of basalt and harzburgite having a basalt fraction of 18%, indicative of a phase change in subducted oceanic crust, which is consistent with the disappearance of garnet. The HeFESTo predicted phase change in the temperature derivative consists of relatively weak peak having a 7 km width.

4.3.2. 250 km: The Mystery of the Lehmann Discontinuity

The inverted heterogeneity peak at 250 km \pm 12 km is neither the orthopyroxene to high pressure clinopyroxene phase change predicted closer to 300 km or the X discontinuity found in many receiver function studies (Pugh et al., 2021). Both of these are too narrow (<10 km) to be detected by stochastic tomography and the filtered HeFESTo predictions shown in Figs. 6bc and 7. We instead interpret this to be a signal associated with the Lehmann discontinuity (Lehmann, 1961). The Lehmann discontinuity is frequently detected in S wave studies at depths 220–240 km beneath continents (e.g., Vinnik et al., 2015). An exception to continental observations, however, is the work of Zheng et al. (2007) who find a 250 km reflector in the Tonga mantle wedge, which they explain by silica enrichment. The 250 km discontinuity is feature of PREM (Dziewonski and Anderson) that separates an anisotropic lithosphere from a more nearly isotropic asthenosphere. Karato (1992) has suggested that the Lehmann discontinuity is associated with a change in rheology and viscosity from dislocation creep above to diffusion creep below a 20 km wide or greater zone centered near 240 km depth for wet and/or hot conditions. This transition is also often associated with the bottom of a low velocity zone for body waves. Unaccompanied by a change in heterogeneity power, however, a change in anisotropy and rheology cannot scatter or affect the

CORMIER ET AL. 8 of 15

coherence of body waves. Vinnik et al. (2005) have also shown that a change in rheology and anisotropy alone cannot account for the sign of the S to P conversion of S waves incident on the Lehmann discontinuity.

A mechanism that may explain the existence of heterogeneity in this depth interval is the hypothesis of Ono (2007), who proposed that the Lehmann is due to the effects of dehydration of subducted oceanic sediments beneath a continent. Given that HeFESTo does not yet include the effects of water, its non-prediction of the 240 km peak in heterogeneity in Figure 7 observed by stochastic tomography may support Ono's hypothesis. The required distribution of heterogeneity may be in the form of trapped interconnected water or melt (e.g., Selway & O'Donnell, 2022). If the Lehmann is due to an abrupt change in the volume of either melting or dehydration, it could also be associated with an abrupt vertical change in the electrical resistivity. Resistivity anomalies resolved in magnetotelluric studies of the uppermost mantle, however, are primarily marked by a sharp increase near 100–150 km rather than 220–240 km (Moorkamp, 2022; Ramirez et al., 2022).

4.4. Limitations in Resolution

The differences between detected and predicted phase changes will depend on the accuracy of the assumptions in the thermodynamic model and the sampling and errors in the power spectrum of heterogeneity determined from stochastic tomography. The depth accuracy of the thermodynamic model depends on the validity of the assumed petrologic model, the physical properties of minerals determined from combinations of experimental observations and ab initio calculations, and the assumed temperature profile (Stixrude & Lithgow-Bertelloni, 2011, 2022). The accuracy of the power spectrum estimated from stochastic tomography largely depends on the depth-sampling rate that can be resolved in the inversion of coherences, which depends on sensor spacing and its geometry and the azimuthal and depth distribution of seismic events (Wu & Xie, 1991).

A global 660 km discontinuity has been largely confirmed in many seismic studies and is generally the most robustly detected discontinuity by reflected body waves having dominant frequencies even approaching 1 Hz (e.g., Deuss et al., 2006). Its signature in receiver functions (Andrews & Deuss, 2008), however, can be complex, in agreement with the complex phase changes predicted from thermodynamic models at and near this depth (Xu et al., 2008). A partial explanation for a positive detection at 600 km but not 660 km is that the 25 km sampling rate in the inversion is simply too coarse to resolve the complex signal of two closely spaced phase changes. Our shallower 600 km deep detection of a phase change is the transformation of high-pressure clinopyroxene to akimotoite initiating closer to 600 km than 650 km. Hao et al. (2019) predict this transition to have a width on the order of 25 km or greater.

4.5. Geotherm Perturbation and Slab Stagnation

The detection of an akimotoite transition at 600 km, indicative of the existence of regions of colder mantle temperatures (Hogrefe et al., 1994), coupled with a phase transition in basalt at 775 km, is consistent with the history of the subduction of the Farallon plate beneath the western US. Tomographic images of the shear velocity structure of the mantle beneath this region reveal evidence of both slab stagnation and fragmentation in the lower mantle transition zone as well as penetration beneath 660 km (Schmid et al., 2002).

Two isothermal runs of HeFESTo (Figure 8) demonstrate the relative sensitivity of different predicted phase transitions to changes in temperature. The 410 and 660 km phase transitions are considerably less sensitive to lateral temperature variations than the wadsleyite to ringwoodite and akimotoite transitions near 500 and 600 km depth, respectively. Hence, if the physical properties and chemistry of these two transitions are well understood, they can potentially serve as accurate thermometers in the transition zone. Assuming that errors in of the chemistry and physical properties taken as inputs to HeFESTo are small, we can estimate the temperature required to make the transition zone phase changes come into better agreement with our measurements of heterogeneity in the transition zone from stochastic tomography. A difference derivative equal to 0.164 km/deg K can be calculated from the shift in depth of the wadsleyite to ringwoodite (wa | ri) phase change for the two temperatures plotted in Figure 8. Using this derivative, a negative 180 K temperature perturbation at 500 km depth is required to bring the depth of wa | ri into agreement with its depth inferred from stochastic tomography. Figure 9 applies this cool temperature perturbation at 500 km, which brings the heterospectrum determined from stochastic tomography for the wadsleyite to ringwoodite transition into agreement with that predicted from HeFESTo. The form of this perturbation is similar to those proposed in mantle convection studies by Tackley et al. (1993) and Matyska and Yuen (2002), who predict non-adiabatic perturbations to the mantle geotherm due to slab stagnation in the

CORMIER ET AL. 9 of 15

from https://agupubs.onlinelibrary.wiley.com/doi/10.1029/2022J B025035 by University of California - Los Ange, Wiley Online Library on [26/06/2023]. See the Terms

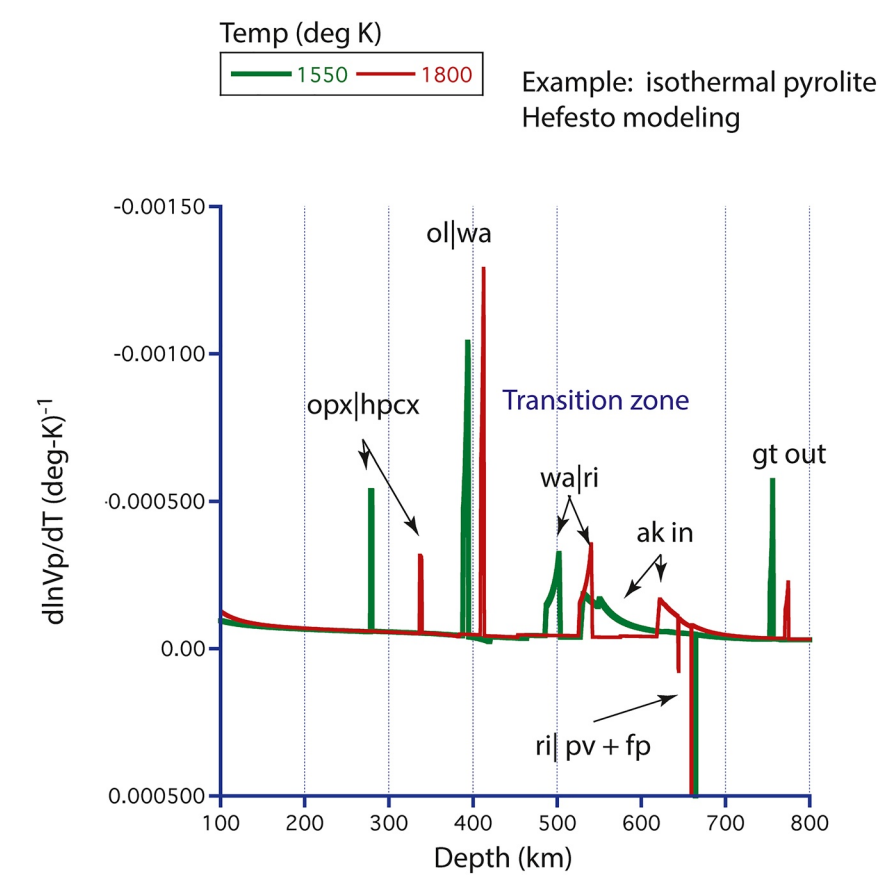


Figure 8. Isothermal calculations of $d\ln Vp/dT$ for pyrolite for 1550 and 1800 K.

transition zone. Tomographic cross-sections of P velocities beneath our region of study also support a cool transition zone due to the subduction of the Farallon slab beneath the western US (e.g., Simmons et al., 2012).

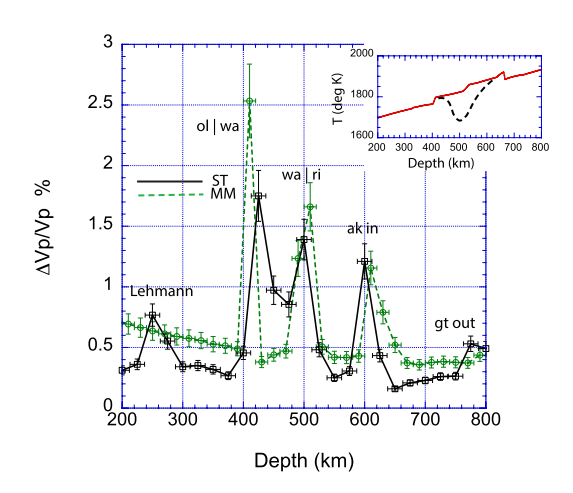


Figure 9. Solid black line (ST): mantle heterogeneity spectrum of *P* waves measured from stochastic tomography applied to the western US. Short green dashed line (MM): temperature derivative calculated from the HeFESTo thermodynamic code for a mechanical mixture of harzburgite and basalt assuming a 180 K negative temperature perturbation at 500 km depth in the mantle transition zone is applied to a 1600 K adiabat (dashed line inset at upper right).

The combination of mechanisms creating slab stagnation are still actively debated, depending on slab rollback at the initial subduction zone, the fine structure of the endothermic phase change near 660 km, its Clapeyron slope, and whether there is a viscosity increase or decrease below the 660 km phase change (e.g., Mao & Zhong, 2008). The non-detection of 660 km phase change from stochastic tomography, its otherwise ubiquitous detection from reflected and converted high frequency (>1 Hz) body waves (e.g., Whitcomb & Anderson, 1970), the narrow width of metamorphic temperature derivatives of its P and S wave velocity changes, and its topography are all consistent with it being an endothermic phase change, very narrow in width (no more than 2–10 km), with a near vertical Clapeyron slope.

5. Conclusions

5.1. Strongest Contribution to Upper Mantle Heterogeneity

From stochastic seismic tomography applied to the upper 1,000 km of the western US, we have shown that its heterogeneity spectrum is characterized by a series of peaks related to narrow intervals of depth in which phase or chemistry changes. We have demonstrated the stochastic seismic tomography can capture higher order phase and chemical changes in the upper mantle that are undetectable from reflection imaging. These peaks, having amplitudes

CORMIER ET AL. 10 of 15



on the order of 1%–2% in P velocity fluctuation, strongly correlate with the majority of predicted phase changes from thermodynamic models of the upper mantle's chemistry and phase. Stochastic tomography has the potential to detect mantle phase changes that do not exhibit changes in seismic velocity and density over short depth intervals. These types of phase changes are characterized by paired changes in velocity gradient over a transition depth that may be equal to or larger than the wavelength of a body wave. Results from a depth-sampling interval of 25 km for the inverted spectrum suggest that many of these phase changes may occur over a range in depth equal to or greater than 25 km. An exception is our non-detection of the phase transition at 660 km, consistent with a transition interval in depth that may be as small as 2 km (0.1 GPa).

5.2. Geotherm and Subduction History

Our interpretation of individual peaks in the heterogeneity spectrum as a function of depth is consistent with a history of subduction and slab stagnation in the upper mantle transition zone between 410 and 660 km depth. This interpretation is based largely on the depth position and temperature dependence of the detected wadsleyite to ringwoodite transition at 500 km depth and the calcium perovskite to ringwoodite transition at 600 km depth. A stochastic tomography detection of a smaller, broad (>20 km wide), phase transition near 250 km is interpreted to be the Lehmann discontinuity, which is unpredicted by the compositions and temperatures considered in our thermodynamic modeling. The depths of the 500, 600, and 775 km phase changes require a negative perturbation of a mantle adiabat in the transition zone, possibly extending below the 660 km phase transition. This cool perturbation is consistent with the predictions of mantle convection suggesting slab stagnation in the transition zone, with the predictions of thermodynamic modeling incorporating perturbations to the geotherm, and with fast P velocities in the mantle transition zone found in 3-D travel time tomography of the western US.

5.3. Processing Thermodynamic Predictions

To detect the thermodynamically predicted changes in mantle silicates with stochastic tomography, we demonstrate that a depth sampling interval of 25 km or less must be achieved. Such a resolution may generally also require an estimation of the amplitude and phase effects of source radiation patterns and source-time functions. Averaging of coherence lags over all pairs of sensors having a common lag distance over a large number of earthquakes arriving from different azimuths will enable heterogeneities having scale lengths on the order of the sensor spacing to be detected and will also tend minimize site effects at the near surface of sensors. The 10–20 km spacing of a growing number of Flex Array experiments of the USArray and the availability of waveforms from three widely separated groups of deep focus earthquakes, having simple source-time functions, makes this high resolution possible for at least the western US. Our location of phase changes represents an average for the western US for depths between 200 and 1,000 km, between latitudes 30°N and 50°N and longitudes 100°W and 125°W. Quantification of lateral variations in these phase changes over smaller regions of the upper mantle will depend on the densities and duration of Flex array experiments and the availability of body wavefronts arriving from different azimuths.

Appendix A: Stochastic Tomography

A1. Coherence Measurement

Transmission fluctuation coherence measurements (Equation A1) are the starting point for stochastic tomography. We consider the recorded fields due to two plane waves, PW1 and PW2. We use $U_1(x_1)$ for the recorded field at x_1 for PW1. Likewise, we use $U_2(x_2)$ for the recorded field at x_2 for PW2. Both fields propagate through the same heterogeneous medium. We also consider their corresponding reference fields (no heterogeneities), $U_{1ref}(x_1)$ and $U_{2ref}(x_2)$, respectively. We can write the seismic fields in amplitude and phase terms, for example, $U_1 = u_1 \exp[i\omega t] = u_1 \exp[i\omega t] = u_1 \exp[i\omega t] = u_{1ref} \exp[i\omega t_{ref}] = u_{1ref} \exp[i\omega t_{ref}]$. Similar representations are applied to PW2. A Rytov approximation provides the relationship between the scattered field and the reference field: $U_1 = U_{1ref} e^{\Psi_1}$. The complex function ψ has a real part, which is the logarithmic amplitude, and an imaginary part, which is the phase (or traveltime) difference with respect to the reference value. In our work, the observables are the ratios of log amplitude and travel time differences (eqs. 1c-d) from those computed in a reference Earth model. Transverse coherence functions are constructed as a function of the lag distance x between pairs of receivers. The brace brackets in Equations A1–A4, define the logarithmic amplitude $\langle u_1 u_2 \rangle$ and $\langle \phi_1 \phi_2 \rangle$ phase

CORMIER ET AL. 11 of 15

coherences by averaging measurements for a specific lag distance over all combinations of two receivers in an array separated by that lag distance. Non-dimensional coherence values range from zero (amplitude and traveltime fluctuations) at neighboring receivers to 1 for perfect correlation of amplitudes and to 2π for perfect correlation of phase.

$$\langle u_1 u_2 \rangle = \frac{1}{2} Re \langle \psi_1 \psi_2^* \rangle + \frac{1}{2} Re \langle \psi_1 \psi_2 \rangle \tag{A1}$$

$$\langle \phi_1 \phi_2 \rangle = \frac{1}{2} Re \langle \psi_1 \psi_2^* \rangle - \frac{1}{2} Re \langle \psi_1 \psi_2 \rangle, \text{ where}$$
 (A2)

$$\psi(\omega) = \ln(u/u_{\text{ref}}) + i\omega(t - t_{\text{ref}})$$
(A3)

$$u = (\psi + \psi^*)/2$$
 and $\phi = (\psi - \psi^*)/2i$ (A4)

To construct the complex function $\psi(\omega)$ and its complex conjugate $\psi^*(\omega)$, we measure u and u_{ref} from observed and synthetic seismograms around the direct P waves from the outputs of a multi-taper filter at 0.7 Hz, and measure the traveltime difference $t-t_{\text{ref}}$ from cross-correlation of observed and predicted reference waveforms.

A2. Inversion for Power Spectrum

Stochastic tomography assumes that the functional behaviors of the coherences with lag distance are due to the interference of plane waves scattered by random heterogeneities having an unknown power spectrum as a function of wavenumber and depth. The transverse coherences can be written as an integral over horizontal wavenumber and depth, with an integrand containing the power spectrum.

$$\langle u_1 u_2 \rangle = (2\pi)^{-1} \int_0^H d\xi a_1(\xi) a_2(\xi) \int_0^\infty J_0[\kappa R(\xi)] \sin[\omega \theta_1(\xi)] \sin[\omega \theta_2(\xi)] P(\xi, \kappa) \kappa d\kappa \tag{A5}$$

$$\langle \phi_1 \phi_2 \rangle = (2\pi)^{-1} \int_0^H d\xi a_1(\xi) a_2(\xi) \int_0^\infty J_0[\kappa R(\xi)] cos[\omega \theta_1(\xi)] cos[\omega \theta_2(\xi)] P(\xi, \kappa) \kappa d\kappa \tag{A6}$$

$$\langle u_1 \phi_2 \rangle = (2\pi)^{-1} \int_0^H d\xi a_1(\xi) a_2(\xi) \int_0^\infty J_0[\kappa R(\xi)] \sin[\omega \theta_1(\xi)] \cos[\omega \theta_2(\xi)] P(\xi, \kappa) \kappa d\kappa \tag{A7}$$

In Equations A5–A7, P is the power spectrum as a function of depth ξ and horizontal wavenumber κ . H is the thickness of a heterogeneous layer. Functions a_1, a_2, θ_1 and θ_2 are defined Zheng and Wu (2008)). a_1, a_2 incorporate the effects of amplitude differences between rays arriving at receivers 1 and 2; θ_1, θ_2 incorporate phase differences between receiver pairs 1 and 2. The function R appearing in the argument of the Bessel function J_0 is the horizontal distance between the pair of rays arriving at a specific lag distance at depth ξ .

These integrals can be discretized and set-up as a linearized inverse problem in which the squared difference of the observed coherences and predicted coherences of an unknown power spectrum are minimized. The discretized forms of eqs.2a-c and the object function to be minimized are given in Appendix B of Cormier et al. (2020).

Appendix B: Waveform Data

The coherence data we chose to invert were three groups of deep focus earthquakes (Marianas, Tonga-Kermedec, and South America) downloaded from the Data Management Center of IRIS (Figure B1). Deep focus events (400–700 km) were chosen to avoid the effects of heterogeneity concentrated in the upper mantle near the source and to eliminate the effects of near source reflections. Waveforms were selected from 21,205 *P* waves from earthquakes in these three groups contained in the Global Centroid Moment Tensor (GCMT) catalog in the time range 1 January 2000 and to 1 October 2017 having moment magnitudes Mw 5.8–6.2, recorded by stations between 30°N and 50°N latitude and 100°W to 125°W longitude. Data included waveforms from more than 26 Flexible Array experiments and regional networks operating in this time period and geographic region, having sensors spaced between 10 and 20 km apart, as well as the Transportable USArray, having sensors spaced 70 km apart. The Flexible Array experiments are described at https://usarray.org/researchers/obs/flexible/deployments.

CORMIER ET AL. 12 of 15

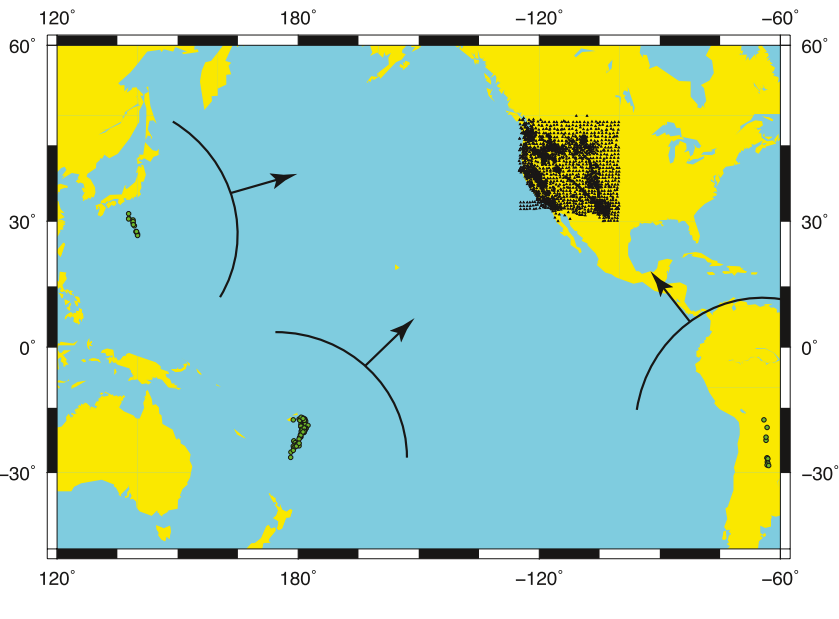


Figure B1. Hypocenters (green dots) of three deep-focus earthquake groups and US and Flex Array seismic stations (black triangles) used in the inversion of *P* wave coherence for the upper mantle heterogeneity spectrum. Clusters of more densely spaced (10–20 km) stations are from more than 20 local networks and Flex Array experiments.

Station and network codes, prefixed to waveform files downloaded from IRIS, can be interpreted from a search tool at https://fdsn.org/networks, maintained by the International Federation of Digital Seismograph Networks.

In pre-processing we removed the instrument response and filtered with a band pass window from 0.3 to 1.5 Hz. Waveforms having a high signal-to-noise ratio were selected by the method described by Johnson & Dudgeon, 1993 with a selection threshold set to 6. About 40% of these had sufficiently high signal to noise ratios and were judged to have simple apparent source-time functions to include in the coherence measurements. Within each earthquake group, measured coherences are averaged over all receiver pairs corresponding to a specific lag. Wavefront healing due to propagation from the source to the teleseismic receivers and averaging coherences at each lag over all earthquakes aid in eliminating any source-side heterogeneity effects. A joint inversion of data comprising three wavefronts arriving from widely different azimuths, whose rays cross at variable depths beneath the array, makes it possible to achieve a sensitivity to heterogeneity scales on the order of the smallest spacing (10 km) of array elements.

The inclusion of the effects of the specific earthquake source-time functions and radiation patterns in u_{ref} are essential to isolating the effects of forward scattering from those of the source. To achieve this for each event the reference synthetic seismogram u_{ref} at each array element was computed from the IRIS Syngine service (Nissen-Meyer et al., 2014; https://service.iris.edu/irisws/syngine) in the AK135-F Earth model (Montagner & Kennett, 1995) using the known moment tensor solution for each event from the GCMT service (Ekstrom et al., 2012; https://www.globalcmt.org) and an empirical source time function determined by stacking P waves from each event in the 40° to 90° distance range. In conjunction with this paper we also provide a link to Python and Matlab scripts to assist researchers in designing experiments with stochastic tomography (Tian & Cormier, 2020). These example scripts treat the effects of earthquake moment tensors and source-time functions on the reference wavefields defining coherence measurements.

Data Availability Statement

Waveform data and services for centroid moment tensors and synthetic seismograms are available from the Incorporated Research Institutions for Seismology through the web site https://www.iris.edu. Matlab and Python scripts for processing and inverting amplitude and phase coherences for single layer and depth dependent heterogeneity spectra are available from the web site listed in the Tian and Cormier (2020) entry in References. The HeFESTo thermodynamic mineral code is described in Appendix B of Stixrude and Lithgow-Bertelloni (2011).

CORMIER ET AL. 13 of 15

Acknowledgments

This study incorporated work funded by the National Science Foundation under Grants EAR 14-46509 (VC), EAR-1900633 (CLB), EAR-1853388 (LS),and EAR 16-21878 and EAR-2027150 (YZ). Figure B1 was drawn using the Generic Mapping Tools (Wessel & Smith, 1998). We thank two anonymous reviewers and Laura Cobden for reviewing and suggesting improvements to our manuscript.

References

- Anderson, D. L. (1989). Theory of the Earth. (Ch. 3). Blackwell.
- Andrews, J., & Deuss, A. (2008). Detailed nature of the 660 km region of the mantle from global receiver function data. *Journal of Geophysical Research*, 113, (B6), B06304. https://doi.org/10.1029/2007JB005111
- Buchen, J. (2021). Seismic velocities in Earth's mantle from mineral elasticity. In H. Marquardt, M. Ballmer, S. Cottar, & J. Konter, (Eds.), Mantle convection and surface expressions. Geophysical Monograph Series. https://doi.org/10.1002/971119528609
- Burdick, L. J., & Helmberger, D. V. (1978). The upper mantle P velocity structure of the Western United States. *Journal of Geophysical Research*, 83 (B4), 1699–1712. https://doi.org/10.1029/jb083ib04p01699
- Cammarano, F., Deuss, A., Goes, S., & Giardini, D. (2005). One-dimensional physical reference models for the upper mantle and transition zone: Combining seismic and mineral physics constraints. *Journal of Geophysical Research*, 110(B1), B01306. https://doi.org/10.1029/2004JB003272
- Chu, R., Schmandt, B., & Helmberger, D. V. (2012). Upper mantle P velocity structure beneath the midwestern US derived from triplicated waveforms. *Geochemistry, Geophysics, Geosystems*, 13(2). https://doi.org/10.1029/2011GC003818
- Chust, T. C., Steinle-Neumann, Dolejs, D., Schuberth, B. S., & Bunge, H.-P. (2017). MMA-EoS: A computational framework for mineralogical thermodynamics. *Journal of Geophysical Research*, 122. https://doi.org/10.1002/2017JB014501
- Cormier, V. F., Tian, Y., & Zheng, Y. (2020). Heterogeneity spectrum of Earth's upper mantle obtained from the coherence of teleseismic P waves. Communications in Computational Physics, 28(1), 74–97. https://doi.org/10.4208/cicp.OA-2018-0079
- Deuss, A., Redfern, S. A. T., Chambers, K., & Woodhouse, J. H. (2006). The nature of the 660 km discontinuity in Earth's mantle from global seismic observations of PP precursors. *Science*, 311(5758), 198–201. https://doi.org/10.1126/science.1120020
- Dziewonski, A., & Anderson, D. L. (1981). Preliminary reference Earth model. *Physics of the Earth and Planetary Interiors*, 25(4), 297–356. https://doi.org/10.1016/0031-9201(81)90046-7
- Ekstrom, G., Nettles, M., & Dziewoski, A. M. (2012). The global CMT project 2004-2010: Centroid moment tensors for 13,017 earthquakes. *Physics of the Earth and Planetary Interiors*, 200–201, 1–9. https://doi.org/10.1016/j.pepi.2012.04.002
- Evans, J. R. (1982). Running median filters and a general despiker. Bulletin of the Seismological Society of America, 72(1), 331–338. https://doi.org/10.1785/bssa0720010331
- Frost, D. J. (2008). The upper mantle transition zone. Elements, 4(3), 171-176. https://doi.org/10.2113/GSELEMENTS.4.3.171
- Hao, S., Wang, W., Qian, W., & Wu, Z. (2019). Elasticity of akimotoite under the mantle conditions: Implications for multiple discontinuities and seismic anisotropies at the depth ~600-750 km in subduction zones. Earth and Planetary Science Letters, 528, 115830. https://doi. org/10.1016/j.epsl.2019.115830
- Hogrefe, A., Rubie, D. C., Sharp, T. G., & Seifert, F. (1994). Metastability of enstatite in deep subducting lithosphere. *Nature*, 372(6504), 351–353, https://doi.org/10.1038/372351a0
- Ishii, T., Huang, T., Myhill, R., Fei, H., Koemets, L., Liu, Z., et al. (2019). Sharp 660-km discontinuity controlled by extremely narrow binary post-spinel transition. *Nature Geoscience*, 12(10), 869–872. https://doi.org/10.1038/s41561-019-0452-1
- Johnson, D. H., & Dudgeon, D. D. (1993). Array signal processing: Concepts and techniques. Prentice Hall.
- Karato, S. (1992). On the Lehmann discontinuity. Geophysical Research Letters, 19(22), 2255–2258. https://doi.org/10.1029/92gl02603
- Katsura, T. (2022). A revised adiabatic temperature profile for the mantle. *Journal of Geophysical Research*, 122(2). https://doi.org/10.1029/2021B023562
- Klimes, K. (2002). Correlation functions of random media. Pure and Applied Geophysics, 159(7–8), 1811–1831. https://doi.org/10.1007/s00024-002-8710-2
- Koroni, M., & Trampert, J. (2015). The effect of topography of upper-mantle discontinuities on SS precursors. *Geophysical Journal International*. 204(1), 667–681. https://doi.org/10.1093/gii/ggy471
- Lehmann, I. (1961). S and the structure of the upper mantle. Geophysical Journal of the Royal Astronomical Society, 4(s0), 124–138. https://doi.org/10.1111/j.1365-246x.1961.tb06808.x
- Li, L., Chen, Y. W., Zheng, Y., Hu, H., & Wu, J. (2019). Seismic evidence for plume-slab interaction by high-resolution imaging of the 410-km discontinuity under Tonga. *Geophysical Research Letters*, 46(3), 13687–13694. https://doi.org/10.1029/2019GL084164
- Mancinelli, N., Shearer, P., & Liu, Q. (2016). Constraints on the heterogeneity spectrum of Earth's upper mantle. *Journal of Geophysical Research*, 121(5), 3703–3721. https://doi.org/10.1002/2015jb012641
- Mao, W., & Zhong, S. (2008). Slab stagnation due to a reduced viscosity layer beneath the mantle transition zone. *Nature Geoscience*, 11, 876–881. https://doi.org/10.1038/s41561-018-0225-2
- Matyska, C., & Yuen, D. A. (2002). Bullen's parameter eta: A link between seismology and geodynamical modelling, Earth. Earth and Planetary Science Letters, 198, 471–493.
- Montagner, J. P., & Kennett, B. L. N. (1995). How to reconcile body-wave and normal-mode reference Earth models? Geophysical Journal International, 135, 229–248.
- Moorkamp, M. (2022). Deciphering the state of the lower crust and upper mantle with multi-physics inversion. *Journal of Geophysical Research*. https://doi.org/10.1029/2021GL096336
- Nissen-Meyer, T., van Driel, M., Stähler, S. C., Hosseini, K., Hempel, S., Auer, L., et al. (2014). AxiSEM: Broadband 3-D seismic wavefields in axisymmetric media. *Solid Earth*, 5(1), 425–445. https://doi.org/10.5194/se-5-425-2014
- Niu, F., Levander, A., Ham, S., & Obayashi, M. (2005). Mapping the subducting Pacific slab beneath southwest Japan with Hi-net receiver functions. Earth and Planetary Science Letters, 239(1–2), 9–17. https://doi.org/10.1016/j.epsl.2005.08.009
- Ono, S. (2007). The Lehmann discontinuity due to dehydration of subducted sediment. The Open Mineralogy Journal, 1(1), 1–4. https://doi.org/10.2174/1874456700801010001
- Pugh, S., Jenkins, J., Boyce, A., & Cottar, S. (2021). Global receiver function observations of the X-discontinuity reveal recycled basalt beneath
- hotspots. Earth and Planetary Science Letters, 561. https://doi.org/10.1016/j.epsl.2021.116813

 Ramirez, F. D. C., Selway, K., Conrad, C. P., & Lithgow-Bertelloni, C. (2022). Constraining upper mantle viscosity using temperature and water content inferred from seismic and magnetotelluric data. Journal of Geophysical Research. https://doi.org/10.1029/2021/B023824
- Sato, H., Fehler, M. C., & Maeda, T. (2012). Seismic wave propagation and scattering in the heterogeneous Earth (2nd ed.). Springer-Verlag. Schmid, C., Goes, S., van der Lee, S., & Giardini, D. (2002). Fate of the Cenozoic Farallon slab from comparison of kinematic thermal modeling
- with tomographic images. *Earth and Planetary Science Letters*, 204(1–2), 17–32. https://doi.org/10.1016/s0012-821x(02)00985-8
 Selway, K., & O'Donnell, J. P. (2022). A small, unextractable melt fraction as the cause for the low velocity zone. *Earth and Planetary Science*
- Selway, K., & O'Donnell, J. P. (2022). A small, unextractable melt fraction as the cause for the low velocity zone. Earth and Planetary Science Letters, 517(1), 117–124. https://doi.org/10.1016/j.epsl.2019.04.012
- Shearer, P. (1991). Constraints on upper mantle discontinuities from observations of long-period reflected and converted phases. *Journal of Geophysical Research*, 96(B11), 18147–18182. https://doi.org/10.1029/91jb01592

CORMIER ET AL. 14 of 15



Journal of Geophysical Research: Solid Earth

- 10.1029/2022JB025035
- Simmons, N. A., Myers, S. C., Johannesson, G., & Matzel, E. (2012). LLNL-G3Dv3: Global P-wave tomography model for improved regional and teleseismic travel time prediction. *Journal of Geophysical Research*, 117. https://doi.org/10.1029/2012JB009525
- Solomon, S. C. (1976). Geophysical constraints on radial and lateral temperature variations in the upper mantle. *American Mineralogist*, 61(7–8), 788–903.
- Stixrude, L., & Ligthgow-Bertelloni, C. (2005). Thermodynamics of mantle minerals I. Physical properties. *Geophysical Journal International*, 162(2), 610–632. https://doi.org/10.1111/j.1365-246x.2005.02642x
- Stixrude, L., & Lithgow-Bertelloni, C. (2007). Influence of phase transformations on lateral dynamics in Earth's mantle. Earth and Planetary Science Letters, 263(1–2), 45–55. https://doi.org/10.1016/j.epsl.2007.08.027
- Stixrude, L., & Lithgow-Bertelloni, C. (2011). Thermodynamics of mantle minerals II. Phase equilibria. *Geophysical Journal International*, 184(3), 1180–1223. https://doi.org/10.1111/j.1365-246X.2010.04890.x
- Stixrude, L., & Lithgow-Bertelloni, C. (2012). Geophysics of chemical heterogeneity in the mantle. Annual Review of Earth and Planetary Sciences, 40(1), 569–595. https://doi.org/10.1146/annurev.earth.36.031207.124244
- Stixrude, L., & Lithgow-Bertelloni, C. (2022). Thermal expansivity, heat capacity and bulk modulus of the mantle. *Geophysical Journal International*, 228(2), 1119–1149. https://doi.org/10.1093/gji/ggab394
- Tackley, P. J., Stevenson, D. J., & Glatzmaier, G. A. (1993). Effects of an endothermic phase transition at 670 km depth in a spherical model of convection in the Earth's mantle. *Nature*, 361, 699–704.
- Tian, Y., & Cormier, V. F. (2020). https://github.com/vernoncormier/stochastic_tomography
- Tkalčić, H., Cormier, V. F., Kennett, B. L. N., & He, K. (2010). Steep reflections from the Earth's core reveal small-scale heterogeneity in the upper mantle. *Physics of the Earth and Planetary Interiors*, 178(1–2), 80–91. https://doi.org/10.1016/j.pepi.2009.08.004
- van Stiphout, A. M., Cottar, S., & Deuss, A. (2019). Receiver function mapping of mantle transition zone discontinuities beneath Alaska using scaled 3-D velocity corrections. *Geophysical Journal International*, 219(2), 1432–1446. https://doi.org/10.1093/gji/ggz360
- Vinnik, L. (2019). Receiver function seismology. Izvestiya, Physics of Solid Earth, 55(1), 12-21. https://doi.org/10.1134/s1069351319010130
- Vinnik, L., Kozlovskaya, E., Oreshin, S., Kosarev, G., Piiponen, K., & Silvennoinen, H. (2015). The lithosphere, LAB, LVZ and Lehmann discontinuity under central Fennoscandia from receiver functions. *Tectonophysics*, 667(23), 189–198. https://doi.org/10.1016/tecto.2015.11.024
- Vinnik, L., Kurnik, E., & Farra, V. (2005). Lehmann discontinuity beneath North America: No role for seismic anisotropy. Geophysical Research Letters, 32(9), L09306. https://doi.org/10.1029/2004GL022333
- Wang, F., Barklage, M., Lou, X., van der Lee, S., Bina, C. R., & Jacobsen, S. D. (2018). HyMaTZ: A python program for modeling seismic velocities in hydrous regions of the mantle transition zone. Geochemistry, Geophysics, Geosystems, 19(8), 2308–2324. https://doi.org/10.1029/2018GC007464
- Wessel, P., & Smith, W. H. F. (1998). New, improved version of the generic mapping tools released. *Eos, Transactions American Geophysical Union*, 79(47), 579, https://doi.org/10.1029/98eo00426
- Whitcomb, J. H., & Anderson, D. L. (1970). Reflection of P'P' seismic waves from discontinuities in the mantle. *Journal of Geophysical Research*, 75(29), 5713–5728. https://doi.org/10.1029/jb075i029p05713
- Wu, R. S., & Flatté, S. (1990). Transmission fluctuations across an array and heterogeneities in the crust and upper mantle. Pure and Applied Geophysics, 132(1–2), 175–196. https://doi.org/10.1007/bf00874362
- Wu, R. S., & Xie, X. (1991). Numerical tests of stochastic tomography. Physics of the Earth and Planetary Interiors, 67(1991), 180–193. https://doi.org/10.1016/0031-9201(91)90069-t
- Xu, F., Vidale, J. E., & Earle, P. S. (2003). Survey of precursors to P'P': Fine structure of mantle discontinuities. *Journal of Geophysical Research*, 108(B1), ETG7-10. https://doi.org/10.1029/2001JB000817
- Xu, W., Lithgow-Bertelloni, C., Stixurde, L., & Ritsema, J. (2008). The effect of bulk composition and temperature on mantle seismic structure. Earth and Planetary Science Letters, 275(1–2), 70–79. https://doi.org/10.1016/j.epsl.2008.08.012
- Zheng, Y., Flanagan, M. P., Lay, T., Flanagan, M. P., & Williams, Q. (2007). Pervasive seismic wave reflectivity and metasomatism of the Tonga mantle wedge. Science, 316(5826), 855–859. https://doi.org/10.1126/science.1138074
- Zheng, Y., & Wu, R.-S. (2008). Theory of transmission fluctuations in random media with a depth dependent background velocity structure. Advances in Geophysics, 50, 21–41.

CORMIER ET AL. 15 of 15